Temporal development of NACA airfoil wake affected by an upstream wake

Majd Armaly, E Varea, C Lacour, Luminita Danaila, B Lecordier

15th International Symposium on Particle Image Velocimetry – ISPIV 2023
June 19–21, 2023, San Diego, California, USA

Temporal development of NACA airfoil wake affected by an upstream wake

M. Armaly[1*], E. Varea[1], C. Lacour[1], L. Danaila[2], B. Lecordier[1]

[1] CORIA UMR 6614, University of Rouen Normandy and INSA Rouen, Saint Etienne du Rouvray, France

[2] M2C UMR 6143, University of Rouen Normandy, Mont Saint Aignan, France

[*] Majd.armaly@coria.fr

Abstract

The study aims to uncover the consequence of the wake behind an obstacle by passing another object placed downstream. This issue pertains to wind turbine parks. A simple example is the interaction of a wake behind a cylinder and a blade placed downstream. The wake comprises coherent motions (CM) and random motion (RM). Coherent structures, reminiscent of the Von Kàrmàn street, are created by the obstacle and interact with random motion (RM), thus inducing locally enhanced turbulent cascade and impacted by any possible obstacle in the wake. 2C-2D in-plane velocity fields (190k images) are measured behind the obstacles (Cylinder -Blade) by high-speed Particle Image Velocimetry (H-PIV) to visualize the temporal development. Then, the lock phases numerical method is developed for further statistical studies. The measurement plane is at the center of the test section, with three different local Reynolds numbers based on the cylinder diameter, i.e., Re = 2000, 4000, and 8000.

1 Introduction

Disasters of turbulence on their structures are further highlighted by aerodynamic engineers, as in aircraft, wind turbine parks, or buildings. For instance, the study of Medici and Alfredson (2005) highlighted low-frequency vortices shed from turbines, with a specific frequency due to the turbine wake meandering. The repetitive events of energetic turbulence are known finally in causing structures failure. In turbulence research, wakes behind obstacles have been studied for decades. Roshko (1954) used his measurements based on velocity fluctuation to define flow regimes and vortex shedding behind a cylinder, confirmed by Bloor and Gerrard (1966) and Williamson (1996). Two obstacle studies got attention further, where Igarashi (1981) investigated the flow characteristics around two cylinders. The wake behind obstacles comprises coherent motions (CM) and random motion (RM). Coherent motions in wakes are large-scale eddies that contain the energy of the smaller eddies, as shown in Cerbus and Goldburg (2016). The classical postulates of turbulence are based upon the cascade concept, i.e., kinetic energy is injected at the largest scales of the flow and transferred to smaller scales through the cascade process. Furthermore, the turbulent kinetic energy budget is illustrated by Townsend (1976) to highlight the exchange between the mean and the fluctuations (CM & RM).

Coherent motion (CM), reminiscent of the Von Kármán street, is created by the first obstacle and interacts with RM, thus inducing a locally enhanced turbulent cascade and impacting any possible obstacle in the wake. The interest of the temporal study is to reveal the role of the shedding vortices created by the first obstacle (a cylinder), and their development or deformation by hitting any other obstacle downstream (blade). As a further simplification, we focus on assessing the dynamical behavior of a subsequent wake downstream (the wake of NACA airfoil) as a function of upstream flow. The study of Armaly et al. (2022b) shows the exchange of turbulent kinetic energy over a blade in TBL (Turbulent Boundary Layer) as a function of the upstream flow. It was investigated with a low-speed PIV system comprising four high-resolution PIV cameras to reach high spatial resolution and ensure an excellent statistical convergence. Conversely, the current and complementary study focuses on the temporal aspect of wake interactions to get a clear overview of the shed vortices since its collision with the NACA airfoil. The present contribution shows the power spectrum and temporal correlations as an initial step. A conversion methodology from temporal to phase-lock-based

data is also shown and used for further statistical approach (far aim study). Data transformation helps statistically compare the turbulent kinetic energy with the study of Armaly et al. (2022b). Section 2 describes the experimental setup. Sections 3 and 4 show temporal-based and phase-based results, respectively. Conlusion is in section 5.

2 Experimental setup and data processing

2.1 Wind tunnel and time resolved PIV set-up

The measurements were carried out in a laminar closed circuit wind tunnel at CORIA laboratory operating up to 16 m/s with a very low residual turbulence intensity ($< 1\%$). The wind tunnel has a transparent test section (Length: 2 m - Cross-section: 400×400 mm^2) on all four sides to allow extensive use of optical techniques. Thus, two components of in-plane velocity fields are measured behind the obstacles (Cylinder-Blade) by Particle Image Velocimetry (PIV). The distance between the center of the cylinder (10 mm diameter) and the center of rotation of the airfoil (NACA 0015 profile and 400 mm length) is set to 130 mm with a pitch angle 10°. Capturing the temporal development of long field views downstream the obstacles (360×75 mm^2) leads to setting up an optical arrangement of three high-speed cameras ($f_{max} = 20$ kHz) in a side-by-side configuration. Cameras and the corresponding imaging reflecting mirrors are installed under the test section to visualize the field of view from the bottom side, as shown in Fig.(1). The side-by-side camera setup requires a view overlap (1cm) between camera images to conserve continuity in the field of view. The three successive views are then combined with the help of a large calibration grid which permits the cancellation of optical distortion. The cameras are equipped with lenses with a magnification of 10 $pixels/mm$. A double cavity high-speed Nd-YAG laser (532 nm) of 50 kHz maximum frequency and a power of 15 $mJ/pulse/cavity$ is used to illuminate the vast field of view from the downstream side of the wind tunnel. Both cavities are linked to the same trigger cable leading to the discharge of the cavities simultaneously and illuminating the test section simultaneously (single frame mode). Laser sheets high superposition coefficient helps avoid zones with different intensities at an instant image. Images are acquired in time series mode and processed by the PIV algorithm. The time between images is adapted to increase the dynamical velocity range of measurements, as shown in the study of Jeon et al. (2014).

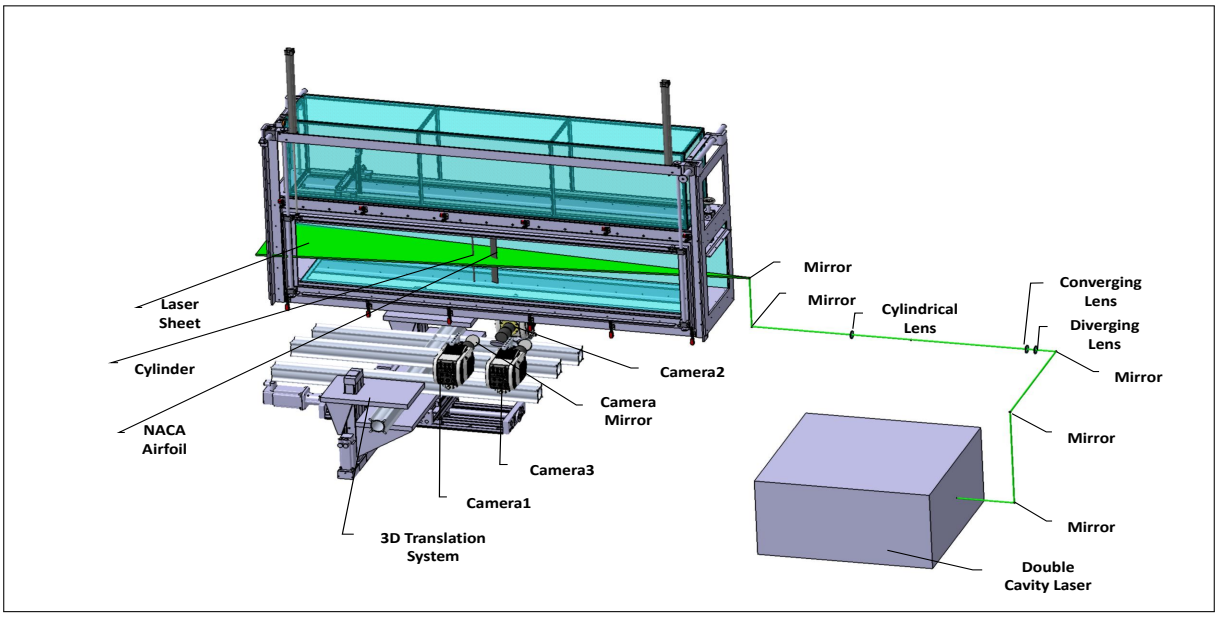

Figure 1: Experimental set-up

The acquisition rate is highly dependent and influenced by the vortices' mean flow velocity and the shedding frequency. For instance, Reynolds numbers based on cylinder diameter of 2000 (3 m/s), 4000 (6 m/s), and 8000 (12 m/s) are optimized to acquisition rates of 5,10 and 20 kHz in single frame mode,

(equivalent to $\Delta t = 200\ \mu s$, $100\ \mu s$ and $50\ \mu s$ in double frame mode, respectively). This helps preserving the excellent image quality and high dynamical behavior of wakes far away from obstacles. Table. 1 shows the experiment parameters of the present contribution. To create the light sheet, the laser beam passes through a cylindrical lens (f = -75mm), spherical lens (f = 150mm), cylindrical lens (f = -50mm), and reflection mirrors. The set of diverging and converging lenses is to enlarge the diameter of the laser beam (beam expander) for a thinner and focused laser sheet. The cylindrical lens diverges the light to illuminate the test section. However, the laser sheet is prevented from lighting the zone between the two obstacles due to the existence of the airfoil.

Experiment parameters				
Re number	St number	Shedding freq. (Hz)	No. periods	No. images
Re = 2000	0.2	60	2280	190K

Table 1: Parameters of the experiment.

2.2 PIV processing

The PIV calculation on the images is entirely based on processing codes developed in the CORIA laboratory [Lecordier and Trinite (2004)], which are continuously improved and adapted to specific situations.
Before the PIV computation, the first step consists in recombining the view of the three cameras into a single image. To perform it, spatial calibration of each camera is performed from the recording of a point pattern grid covering the entire field of view. The camera models are based on third-order 2D polynomial functions to compensate for any view tilt and image distortion. Concerning the image reconstruction, PIV interpolation scheme with image deformation is used, proven to be compatible with sub-pixel techniques for the velocity measurements (Lecordier and Trinité (2006)). An illustration of the image reconstruction processing of the calibration grid is shown in Fig. 2. The three camera field of views are marked with rectangles of different colors. The rectangles show the image overlaps of the common areas (around 1 cm) to ensure the continuity of the velocity field measurement. During the image reconstruction, constant offset of 120 pixel/cm is imposed in both directions, which leads to a slight magnification of the initial image resolution.

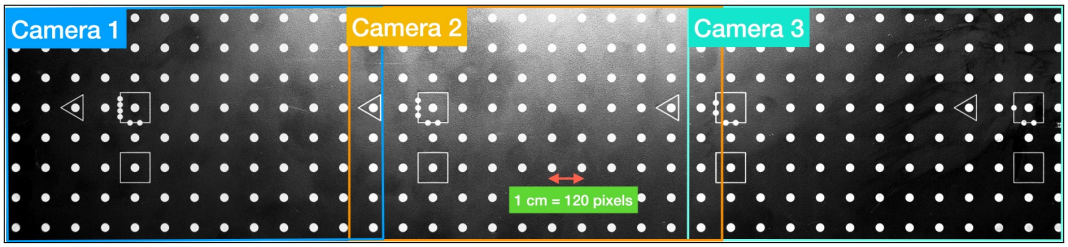

Figure 2: Reconstruction of a complete image from the three camera views of the calibration grid - Final image size: 4256x934 pixels - Imposed image resolution: 12 pixels/mm.

The PIV processing starts with a background correction of images using an averaged image computed over each time sequence. In the present work, the PIV algorithm with image deformation has been retained to improve spatial resolution and maintaining a reasonable computing time. Indeed, even if our high-speed recordings are well suited to temporal algorithms, computation times differ from the amount of data to be analyzed and could only be considered for partial periods of the full-time sequences. The initial interrogation window size is fixed to $32 \times 32\ pixels^2$ ($2.66 \times 2.66\ mm^2$) and is progressively reduced to $16 \times 16\ pixels^2$ ($1.33 \times 1.33\ mm^2$) with 50% of overlap during the deformation process. The final size of the vector grid is 529×113 nodes. Intermediate velocity fields during the process are calculated using a continuous window shift approach (Lecordier and Trinite (2004)), which offers high accuracy with a low addition computational cost compared to the classical PIV algorithm, enabling rapid convergence of the deformation process. The number of iterative steps for the deformation is dynamically adapted from the flow properties of intermediate

predictors, on average is equal to 3. The PIV algorithm uses a masking technique for areas not to be calculated, which avoids instability phenomena on image edges and the boundaries of areas without particles (e.g., obstacle, shadow zone upstream of the second obstacle). All the velocity fields are scaled and validated with a final validation rate higher than 98%. A practical information can be added, that the computation time for a whole time sequence of 190,000 images (38 s at 5 KHz) is around four days on a recent bi-processor Linux cluster with 96 cores.

2.3 Wake phase detection for phase lock analysis

As mentioned in the previous sections, one of the aims of this study is to characterize the flow downstream of the second obstacle as a function of the phase of the coherent structures produced by the first obstacle. An essential analysis element is then determining the phase of production of the pseudo-periodic structures produced by the first obstacle (cylinder or airfoil). The first solution tested was to place a high-sensitivity microphone fitted with a capillary tube in the wake of the first obstacle (Armaly et al. (2022a)). By analog processing of the pressure signal, the value of phase analysis was possible, and all the advantages over a simple statistical approach have been demonstrated. However, the microphone approach has several drawbacks. Firstly, despite of being a small probe it is still affecting the wake. Secondly, the microphone position is fixed untill the PIV images are recorded. For further simplification, phase-lock analysis can be exclusively based on the structures generated by the first obstacle, otherwise microphone position should be changed. Finally, using the microphone proved to be very risky in the airfoil case, as the pressure variations were smaller than for the cylinder, so phase detection presented a significant uncertainty.
Following the previous remarks, a phase detection approach directly from the velocity fields has been developed. This choice is the more relevant with long-term time recordings (38s - 190,000 velocity field at each run). Considering a large number of recorded periods (more than 2,300 per record), phase-lock statistics and temporal analyzes of interactions are accessible. Processing to determine the phase of instantaneous velocity fields involves several steps. The first phase determines a reference velocity field that comprises all instantaneous velocity components into the same phase. An instantaneous velocity field is selected from a series (see the top view of Fig. 3) as the process onset. Each of the selected instantaneous field in the series is correlated with the reference field, limiting the calculation to the area where the CM are most intense (Fig. 3 red frame). When the normalized correlation coefficient between the two fields reaches a certain magnitude, the two velocity fields are considered to have sufficient similarities leading to one identical phase. Note that, only spanwise velocity component v is used in the correlation calculation. Over 190,000 velocity fields of one-time series, nearly 2,000 to 3,000, are identified to be related to the same phase. The average of all the velocity fields provides the reference velocity field for the case of the cylinder and the airfoil (bottom view of Fig. 3). The coherent structures downstream of the obstacle are observable in the two reference fields, as shown in Fig. 3. Remarking that the velocity fluctuations are minimal, indicating good coherent structure detection. The second step is to determine the spatial period between coherent structures using the reference fields corresponding to phase 360°. This is done by a 1D auto-correlation of the velocity component v in stream wise direction in the plane of symmetry of the obstacle is computed (y=0 mm). The oscillation period of the auto-correlation signal allows us to determine the average spatial distance between vortices with high precision. For example, for the two examples shown in Fig. 3, we obtain 40.75 mm and 34.86 mm for the cylinder and airfoil cases, respectively. Once this step is complete, the reference field can be used to determine the phase of the coherent structure of the instantaneous velocity fields.

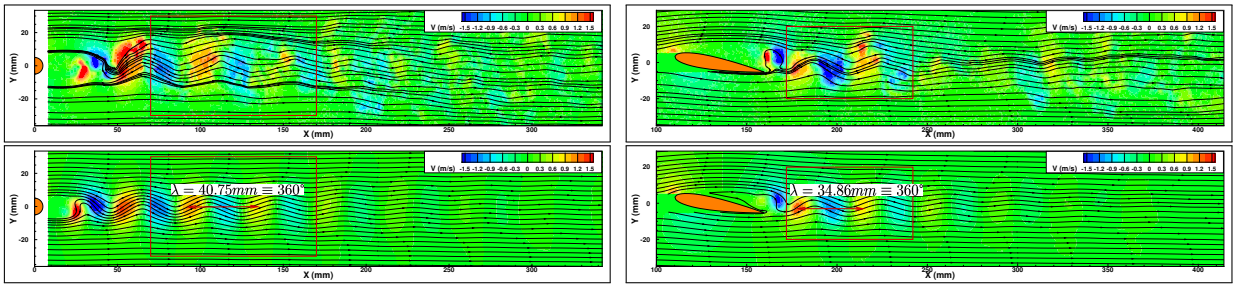

(a) Cylinder case (b) Wing case

Figure 3: Seed (top) and reference (bottom) velocity fields

To detect the phase of structures on an instantaneous velocity field, a normalised correlation coefficient of the spanwise component v of the instantaneous field with the reference field is performed in a restrictive area behind the obstacle (red frame in Fig. 3). This value is calculated for different relative positive and negative field offsets along the x direction. It can be seen as a 2D cross-correlation performed only along one main direction (direction of the main component of the flow). The result is a sinusoidal signal whose position of maxima relative to zero gives the spatial shift between the mean coherent structures of the reference velocity field and the coherent structures of the instantaneous field. The most accurate approach to determining the offset value is to use the zero crossings of this function. An interpolating of the envelope at each crossing is used to improve the measurement of the spatial offset, as it is done in PIV with sub-pixel approach. Knowing the distance between the vortices on the reference field and the spatial offset as described previously, a phase varying in a range of 0 to 360° fields is then assigned to each instantaneous velocity field of the time sequence. To demonstrate the consistency and robustness of the proposed approach, Fig. 4 shows the phase evolution as a function of sample number in the case of the cylinder. A sawtooth signal, characterizing the periodic ejection of coherent structures downstream of the cylinder is measured with a very good regularity, linked to the fundamental frequency given by the Strouhal's frequency of the cylinder. The distribution over 18 phases for the whole time sequence of 38 seconds, shows a satisfactory statistical distribution of the instantaneous fields classification. It is observed with an average of 10,000 instantaneous velocity fields in each phase class.

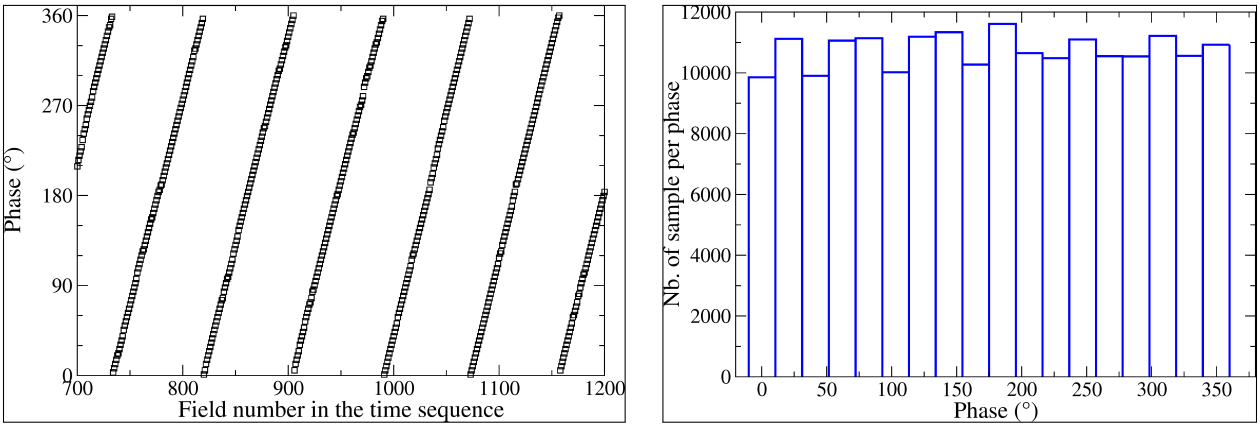

Figure 4: Phase detection in the case of the cylindre - Left: phase as a function of the field number in the time sequence, Right: Phase distribution over a full time record of 38 seconds (190,000 velocity fields)

The final illustration for the rephasing of instantaneous velocity fields is shown in Fig. 5 for the case of a single cylinder. The example shows the entire time sequence that divided into 36 different phases, four are shown in the present study. For the four selected phases, the average coherent structures are very well-identified. Fig. 5 also shows the inversion in phase (sign opposition) of the structures: 0° and 180°, 90°, and 270°, respectively. This illustration shows the ability of our approach to determine the phase behind the cylinder, which also works for the airfoil. It can be noticed that phase detection is usable downstream of the first or second external obstacles, giving great flexibility in the analysis of the wake interactions.

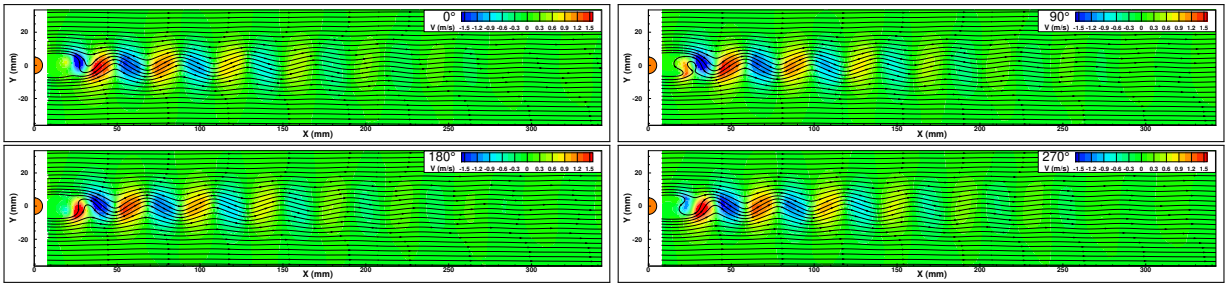

Figure 5: Phase lock reconstruction of the flow behind the cylinder

3 Temporal base results

The quality of the images processing acquired by PIV must be first checked on lower-order statistics, such as the velocity field's mean and Root Mean Square (RMS). Figs 6 and 7 show the RMS of velocity on streamwise (*X/C*) direction and spanswise (*Y/C*) direction perpendicular to the cylinder. RMS is maximum in regions where shear is the most important and gradually decreases downstream behind the cylinder and slightly increased over the blade, as shown in Fig. 6. The upstream wake is highly affected by the leading edge of the airfoil through deviating the wake upwards, as shown in Fig. 7.

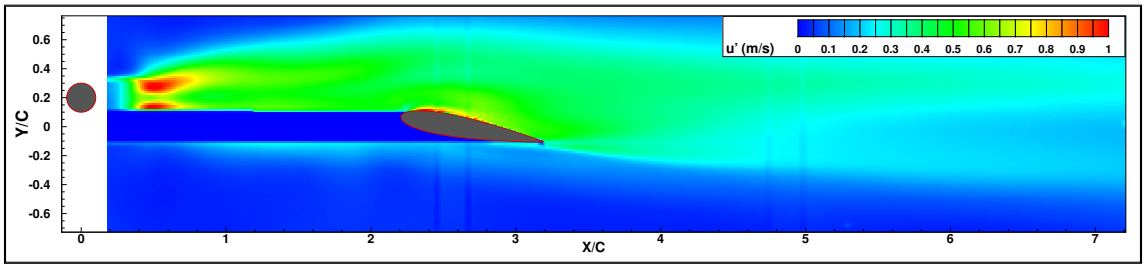

Figure 6: Root Mean Square of velocity fields in streamwise direction, at Re = 2000

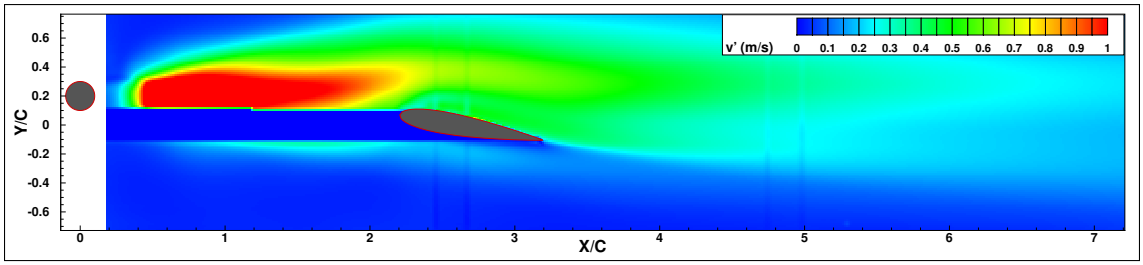

Figure 7: Root Mean Square of velocity fields in spanwise direction, at Re = 2000

Figure 8a shows the time correlations for the spanwise velocity component in a cylinder wake. To compute the correlations, a reference position is fixed at the center of the cylinder wake near-field (*X/D* = 3.5). The positions to be tested in correlation with the reference position are located downstream from the reference point. The correlation coefficients are decreasing to the minimum after 1.6 seconds for all downstream positions. In far fields, generated vortices are still alive, while lower in energy, as shown in Fig. 8a. Fig. 8b shows the power spectrum at different locations downstream the cylinder wake. In the near field, the magnitude of the frequencies is very high, in addition to the harmonics which diminish by moving downstream. The fundamental frequency is close to 60 *Hz* as shown in the table above. The harmonics were also shown by a POD study of Vàclav and Pavel (2020), where the fundamental frequency and the third harmonic frequency have higher amplitudes than the second and the fourth harmonics. In the far field, the power of the vortices frequency (less vortices energy) begins to detract.

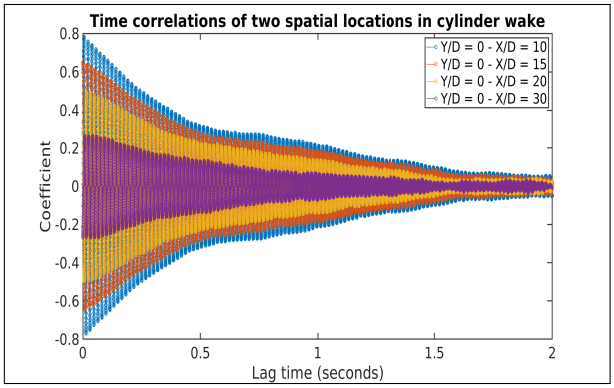

(a)

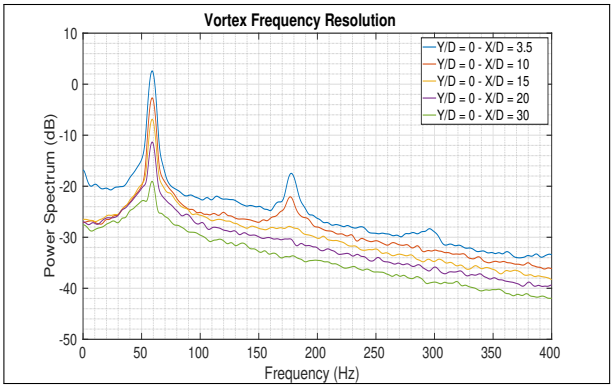

(b)

Figure 8: (a) Time correlations (spanwise velocity component) at the center of the cylinder wake, between a reference point (X/D = 3.5) and 4 different points downstream. (b) Power spectrum (spanwise velocity component) at different locations downstream of the cylinder wake.

Figure 9a shows the time correlations for the spanwise velocity component in an airfoil wake. The reference position is fixed at the center of the airfoil wake near field (X/C = 3.5), and the positions to be tested have an offset of 1 X/C (5cm) downstream. The correlation coefficients are decreasing to the minimum after 0.8 seconds for all downstream positions. This shows that vortices generated by an airfoil have half of the life time of the vortices generated by a cylinder. Figure 9b shows the power spectrum at different locations downstream in the airfoil wake. The fundamental frequency is close to 70 Hz with an existence of the 2nd harmonic frequency, however with an amplitudes much smaller than the cylinder wake.

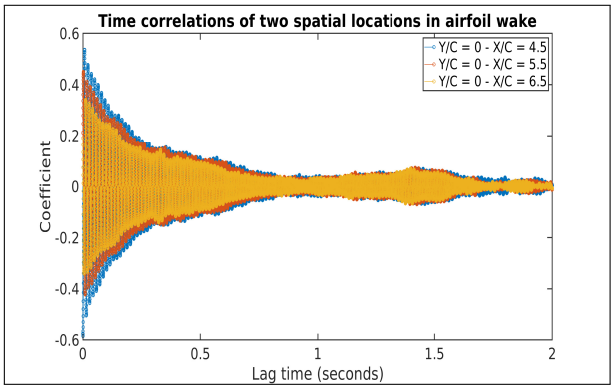

(a)

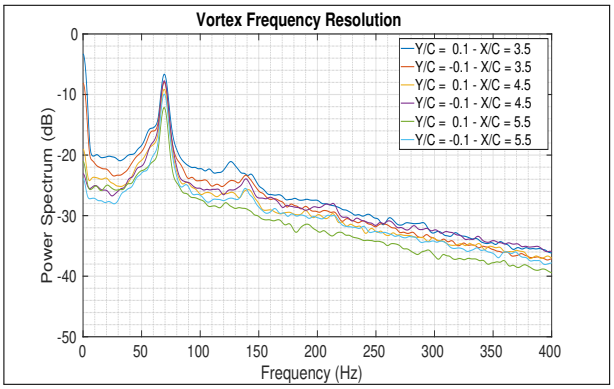

(b)

Figure 9: (a) Time correlations (spanwise velocity component) at the center of the airfoil wake, between a reference point located at X/C = 3.5 and 4 different points downstream. (b) Power spectrum (spanwise velocity component) at different locations downstream of the airfoil wake.

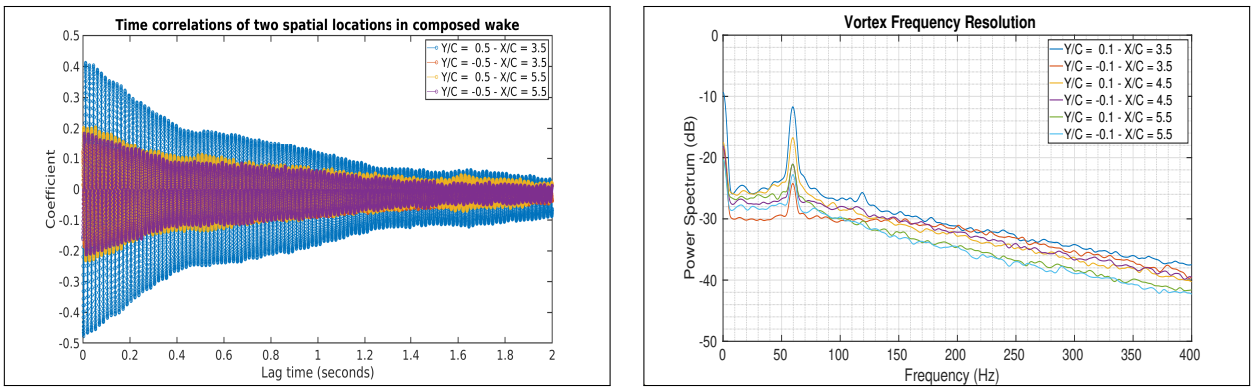

(a) (b)

Figure 10: (a) Time correlations(spanwise velocity component) between a reference point located at *X/D* = 3.5 (*X/C* = 0.7) and 4 different points downstream the airfoil. (b) Power spectrum (spanwise velocity component) at different locations downstream of the composed wake (cylinder + airfoil).

Figure 10a shows the time correlations for the spanwise velocity component in a composed wake (cylinder - airfoil). The reference position is fixed at the upstream wake (cylinder) 's center and X/C = 0.7 (*X/D* = 3.5). The first position in the spanwise direction to be tested in correlation with the reference position is near the leading edge (*Y/C* = 0.1), while the second is near the trailing edge (*Y/C* = -0.1). By comparing the two positions at the same downstream position (*X/C* = 3.5), near the leading edge, the correlation with the cylinder wake is much higher than that of leading edge. This effect might be due to the high generation of vortices from the airfoil's trailing edge. In the far-field region (X/C = 5.5), both positions have a close correlation and are higher from the abovementioned point (*Y/D* = -0.5, *X/D* = 3.5). This shows that the upstream wake simultaneously is correlated with the far-field downstream wake for the same spanwise direction. This behavior is also shown by the power spectrum in Fig. 10b, where all points downstream of an airfoil tend to synchronize with cylinder wake. The downstream points are highly affected by the upstream wake (cylinder) by taking the frequency of the vortices generated in the cylinder wake.

4 Conclusion

The role played by a cylinder wake on a downstream wind turbine airfoil wake is revealed using high-speed temporal PIV. The contribution discusses three wakes: cylinder, airfoil, and composed (cylinder + airfoil) with low Reynolds number $Re = 2000$. The study aims to assess the time correlations at different positions in the wakes and compare their behavior. We have highlighted highly energetic vortices of the cylinder wakes compared to the airfoil wake. The power spectrum is also presented at different positions in the wakes and shows the high dominance of the cylinder vortices in the composed wake. For further objectives, the temporal base data are converted to phase-lock base data by home developed approach as explained above.

Acknowledgements

This work was funded by the French National Research Agency (ANR) under the contract DYNEOL, no. ANR-17-CE06-0020

References

Armaly M, Varea E, Lacour C, Danaila L, and Lecordier B (2022a) Dynamics and phase decomposition in a cylinder wake. in *25th Congrès Français de Mécanique - 25CFM, Nantes, France, September 2022*

Armaly M, Varea E, Lacour C, Danaila L, and Lecordier B (2022b) Turbulent Kinetic Energy Budget and Dynamics of Composed Wakes in TBL. in *23rd Australasian Fluid Mechanics Conference - 23AFMC, Sydney, Australia, December 4-8*

Bloor MS and Gerrard J (1966) Measurements on turbulent vortices in a cylinder wake. *Journal of Fluid Mechanics*

Cerbus RT and Goldburg WI (2016) Information theory demonstration of the richardson cascade

Igarashi T (1981) Characteristics of the flow around two circular cylinders arranged in tandem. *Bulletin of the JSME* 24:532–582

Jeon Y, Chatellier L, and David L (2014) Fluid trajectory evaluation based on an ensemble-averaged cross-correlation in time-resolved piv. *Experiments in Fluids* 55:1766

Lecordier B and Trinite M (2004) Advanced piv algorithms with image distortion validation and comparison using synthetic images of turbulent flow. in *Particle Image Velocimetry: Recent Improvements*. pages 115–132. Springer

Lecordier B and Trinité M (2006) Accuracy assessment of image interpolation schemes for piv from real images of particle. in *Proceedings of the 13th International Symposium on Applied laser techniques to fluid mechanics, Lisbon, Portugal*

Medici D and Alfredson P (2005) Measurements on a wind turbine wake: 3d effects and bluff body vortex shedding. *Wind Energy* 9:219–236

Roshko A (1954) On the development of turbulent wakes from vortex street. *National Advisory committee for aeronautics*

Vàclav U and Pavel P (2020) POD Spectrum of the Wake behind a Circular Cylinder. in *International Scientific Conference – The Application of Experimental and Numerical Methods in Fluid Mechanics and Energy*. volume 328

Williamson C (1996) Vortex dynamics in the cylinder wake. *Journal of Fluid Mechanics* 28